



# Ferroelectric and magneto-dielectric properties of yttrium doped $\text{BaTiO}_3\text{--CoFe}_2\text{O}_4$ multiferroic composite

Mehraj Ud Din Rather<sup>1</sup> · Rubiya Samad<sup>1</sup> · Basharat Want<sup>1</sup>

Received: 19 April 2018 / Accepted: 11 September 2018 / Published online: 15 September 2018  
© Springer Science+Business Media, LLC, part of Springer Nature 2018

## Abstract

Multiferroic composites of ferroelectric and ferrite phases having general formula  $x\text{CoY}_{0.1}\text{Fe}_{1.9}\text{O}_4\text{--}(1-x)\text{Ba}_{0.95}\text{Y}_{0.05}\text{TiO}_3$  (where  $x = 0.05, 0.1$  and  $0.15$ ) were prepared using the conventional solid-state reaction method. X-ray diffraction studies were done to confirm the presence of constituent phases. The microstructural analysis revealed an increase in density with the increase of ferrite content in the ferroelectric matrix. Dielectric studies of the composites, in the temperature range 100–550 K revealed two ferroelectric phase transitions. Variation of dielectric constant and dielectric loss with frequency in the range of 20–3 MHz was carried out at room temperature. The low-temperature dc conductivity behaviour follows Mott's law, confirming the variable range hopping mechanism in all the composites. All the composites showed P–E and M–H hysteresis loops; which confirm the ferroelectric and ferrimagnetic nature of the composites. At temperatures below 173 K, an increase in coercivity and saturation magnetization is observed due to frozen spins. The coupling between ferroelectric and ferromagnetic ordering was confirmed by room temperature magneto-dielectric studies. The decrease in real part of dielectric constant and dielectric loss was observed with an increase in the applied magnetic field. An appreciable increase in percentage magneto-capacitance was observed at lower frequencies and with the increase of ferrite content in the composites. The magneto-electric coupling coefficient was calculated by using the expansion of the thermodynamic potential  $\phi$  (for  $x = 0.15$ ) and was found to be  $3.397 \times 10^{-2} \text{ (emu/g)}^{-2}$ .

## 1 Introduction

Multiferroic materials, which simultaneously combine ferroelectric and ferromagnetic properties, have gained tremendous attention within the scientific community. These multifunctional materials, combining several useful properties in the same substance, produce new phenomena that are technologically important. In these systems, the coupling between ferroelectric and ferromagnetic properties could lead to an electric-field switchable magnetization or vice-versa. The multifunctional behaviour of multiferroic materials provides significant potential for applications such as spintronics, memory, and sensors to the next-generation devices [1–3].

The multiferroic materials are of two types which include single phase and biphasic composites. In the single phase materials, both the ferroic orders exist within the same phase

such as  $\text{BiFeO}_3$ ,  $\text{BiMnO}_3$  and  $\text{YMnO}_3$ . The drawbacks of single-phase multiferroic compounds include the chemical incompatibility of the materials, the existence of a weak coupling between the order parameters at room temperature, and difficulty in tuning the magnetoelectric (ME) response [4–6]. In comparison to single phase, in biphasic multiferroic materials, the ME effect is a product property arising due to both the ferroic orders present in the composite. The extra degrees of freedom due to the coupling between the various order parameters enable them to be useful in various scientific and technological applications [6].

Among ferroelectrics, barium titanate (BT) having cubic perovskite structure is preferred as it is non toxic and has lead free chemical composition unlike lead zirconium titanate. It is an important material for tunable microwave devices due to its high dielectric constant, low dielectric loss and can be operated at high electric fields. Further, it is ferroelectric in the wide temperature range (from 400 to 30 K) which can also be varied by doping  $\text{BaTiO}_3$  with rare-earth elements [7–9]. On the other hand, the chemical stability, Curie temperature and magneto-crystalline anisotropy ( $2.1\text{--}3.9 \times 10^6 \text{ ergs/cm}^3$ ) of  $\text{CoFe}_2\text{O}_4$  (CFO) is high. Also the

✉ Basharat Want  
basharatwant@gmail.com

<sup>1</sup> Solid State Research Lab, Department of Physics, University of Kashmir, Srinagar 190006, India

high magnetostriction of CFO makes it a proper candidate for multiferroics [10]. In addition to these favorable properties of individual phases, an important advantage of multiferroic composite fabricated from BaTiO<sub>3</sub> and CoFe<sub>2</sub>O<sub>4</sub> phases is the spinodal decomposition, which prevents any chemical reaction between these phases at high temperature sintering.

So far, a lot of research has been done on BT-CFO multiferroic composite ceramics. Yang et al. employed one pot solid-state reaction method to investigate the structural, magnetic and magnetodielectric behaviour of the BT-CFO multiferroic composite [11]. The structural, dielectric, ferromagnetic, ferroelectric and ac conductivity studies of the BaTiO<sub>3</sub>-CoFe<sub>1.8</sub>Zn<sub>0.2</sub>O<sub>4</sub> multiferroic particulate composites have been reported in the literature [12]. Apart from ferroelectric and magnetic properties, Etier et al. also studied the converse magnetoelectric effect of the CoFe<sub>2</sub>O<sub>4</sub>/BaTiO<sub>3</sub> composite ceramics sintered from core/shell CoFe<sub>2</sub>O<sub>4</sub>/BaTiO<sub>3</sub> nanoparticles [13].

Although a lot of research is going on multiferroic composites based on titanates and spinel ferrites, the research on multiferroic composites, in which separate ferroic phases are doped with rare-earth elements, is not prominent in the literature. As reported in the literature, the dielectric constant is enhanced, Curie temperature is shifted towards room temperature and the dielectric loss is minimized by yttrium doping in the individual ferroic phases [7, 14–16]. Keeping this in view, we incorporated yttrium in both the ferroelectric and ferrite phases of the composite.

The composites can be prepared by solid state reaction method [17, 18] and by sol-gel auto combustion technique [19, 20]. In the present study, we have fabricated the  $x\text{CoY}_{0.1}\text{Fe}_{1.9}\text{O}_4-(1-x)\text{Ba}_{0.95}\text{Y}_{0.05}\text{TiO}_3$  composite ceramics (where  $x=0.05, 0.10$  and  $0.15$ ) by using solid-state reaction method. This method was preferred in order to obtain dense microstructures, which is a basic route to enhance interaction between grains of two ferroic phases in composites. In addition to the structural, dielectric, ferroelectric and magnetic properties discussed earlier in literature [11–13], the ferrite concentration dependence of ferroelectric and magneto-dielectric properties have been investigated in detail.

## 2 Research material and experimentation

Multiferroic composites with chemical formula  $x\text{CoY}_{0.1}\text{Fe}_{1.9}\text{O}_4-(1-x)\text{Ba}_{0.95}\text{Y}_{0.05}\text{TiO}_3$  (where  $x=0.05, 0.10$  and  $0.15$ ) were prepared by conventional solid-state route. For the preparation of Ba<sub>0.95</sub>Y<sub>0.05</sub>TiO<sub>3</sub> (YBT) ferroic phase, equimolar amounts of BaCO<sub>3</sub> (99.95%), TiO<sub>2</sub> (99.9%) and Y<sub>2</sub>O<sub>3</sub> (99.9%) were mixed thoroughly using acetone as mixing medium. The mixed powders were calcined at 1100 °C for 3 h with the heating rate of 5 °C/min. The calcined

powder was then grounded for 3 h and sintering was done at 1200 °C for 12 h.

The analytical grade chemicals including ferric nitrate nonahydrate, strontium nitrate anhydrous and anhydrous citric acid were used for the preparation of CoY<sub>0.1</sub>Fe<sub>1.9</sub>O<sub>4</sub> (YCFO) phase. All the metal nitrates and citric acid were dissolved in de-ionized water separately. The resulting solutions were mixed together at room temperature and to maintain the PH of the solution at 7, ammonia solution was added to the mixture drop by drop. The gel formation was ascertained by heating the solution at 90 °C for 1 h and the resulting gel was heated till combustion occurs. The ashes left after combustion were grounded in a motor and pestle for about 1 h and the resulting powder was sintered at 900 °C for 4 h for proper phase formation. For the preparation of  $x\text{CoY}_{0.1}\text{Fe}_{1.9}\text{O}_4-(1-x)\text{Ba}_{0.95}\text{Y}_{0.05}\text{TiO}_3$  composites ( $x=0.05, 0.10$  and  $0.15$ ), equivalently denoted as YBC1, YBC2 and YBC3 respectively, the YBT and YCFO phases by weight were mixed in an agate mortar for 4 h. The prepared YBT, YCFO phase as well as YBC1, YBC2 and YBC3 composites were pressed into pellets having 13 mm and 8 mm diameter by using (3–6 wt%) polyvinyl alcohol (PVA) as a binder. A constant pressure of 155 kg/cm<sup>2</sup> was used from an automatic KBr press for pellet formation. In order to evaluate the various properties, the resulting mixture in pellet form was sintered at 1150 °C for 4 h in alumina crucible trays.

## 3 Property measurements

The crystalline phases of all the composites were determined by using a laboratory diffractometer with Cu K<sub>α</sub> ( $\lambda = 1.5406 \text{ \AA}$ ) radiation. X-ray diffraction (XRD) data were collected in the range of  $2\theta = 10 - 90^\circ$  in the steps of  $0.02^\circ$  with a duration of 6.0 s per step. The in-depth external morphology of the prepared samples was studied by using a Field Emission Gun-Scanning Electron Microscope (Zeiss Supra 40). The variations of the dielectric constant ( $\epsilon'$ ) and dielectric loss ( $\tan \delta$ ) with frequency at room temperature in the range of 20–3 MHz were studied by using Agilent 4284A precision LCR meter. The variation of  $\epsilon'$  and  $\tan \delta$  over a temperature range of 100–550 K was studied by the LCR meter connected to a microprocessor-based furnace fitted with a temperature controller and a specially designed two-terminal sample holder. The P–E hysteresis loops were traced by using P–E Loop Tracer, Radiant Technologies–Inc. From the ferroelectric hysteresis loops, the various ferroelectric parameters such as saturation polarization ( $P_s$ ), remnant polarization ( $P_r$ ) and Coercive field ( $E_c$ ) were extracted. The magnetic properties like saturation magnetization ( $M_s$ ), remnant magnetization ( $M_r$ ) and magnetic coercive field ( $H_c$ ) were obtained at room temperature from M–H hysteresis

loops by using a vibrating sample magnetometer (Micro Sense EZ9 VSM, USA). In order to ascertain the multiferritic behaviour of all the composites, the magnetodielectric measurements were carried out by a combined setup of VSM and LCR meter. The room temperature magneto-capacitance of silver coated pellets (area = 132 mm<sup>2</sup> and thickness = 0.8 mm) was measured from LCR meter by using a horizontal uniform magnetic field ( $-20 \leq H \leq 20$  kOe) from the VSM.

## 4 Experimental results and discussion

### 4.1 Phase composition

Figure 1(a–e) shows the X-ray diffraction patterns of YBT ferroelectric-phase, YCFO ferrite-phase and YBC1, YBC2 and YBC3 composites, respectively. The XRD patterns of YBT and YCFO phases clearly show that these phases have retained their perovskite and spinel structures respectively.

The peaks corresponding to YBT and YCFO phases are marked by ‘\*’ and ‘■’ respectively. The lattice constants ‘*a*’ and ‘*c*’ determined from XRD data for YBT are 3.996 and 4.032 Å respectively. A slight increase in ‘*a*’ while as a favorable decrease in ‘*c*’ is observed than theoretical values of pure BaTiO<sub>3</sub> [21]. The change in lattice parameters in YBT is attributed to the fact that ionic radius of Y<sup>3+</sup> ion replacing Ti<sup>4+</sup> ion is large, hence replacement of Ti<sup>4+</sup> by Y<sup>3+</sup> ions results in expansion of the unit cell [22].

In composites, two well-defined sets of diffraction peaks denoted by ‘\*’ and ‘■’ were observed which characterize the YBT and YCFO phases respectively. In addition to the two ferroic phases coexisting in the composite, an extra peak denoted by ‘○’ is observed in YBT phase and composites (YBC1 and YBC2), which is due to extra phase (YBa<sub>3</sub>Ti<sub>2</sub>O<sub>8.5</sub>) formed during the fabrication of YBT phase at a sintering temperature of 1200 °C [23]. However due to the higher weight content of YCFO magnetic phase in YBC3, this peak is not observed. The phase fractions of individual ferroic phases in the YBT-YCFO

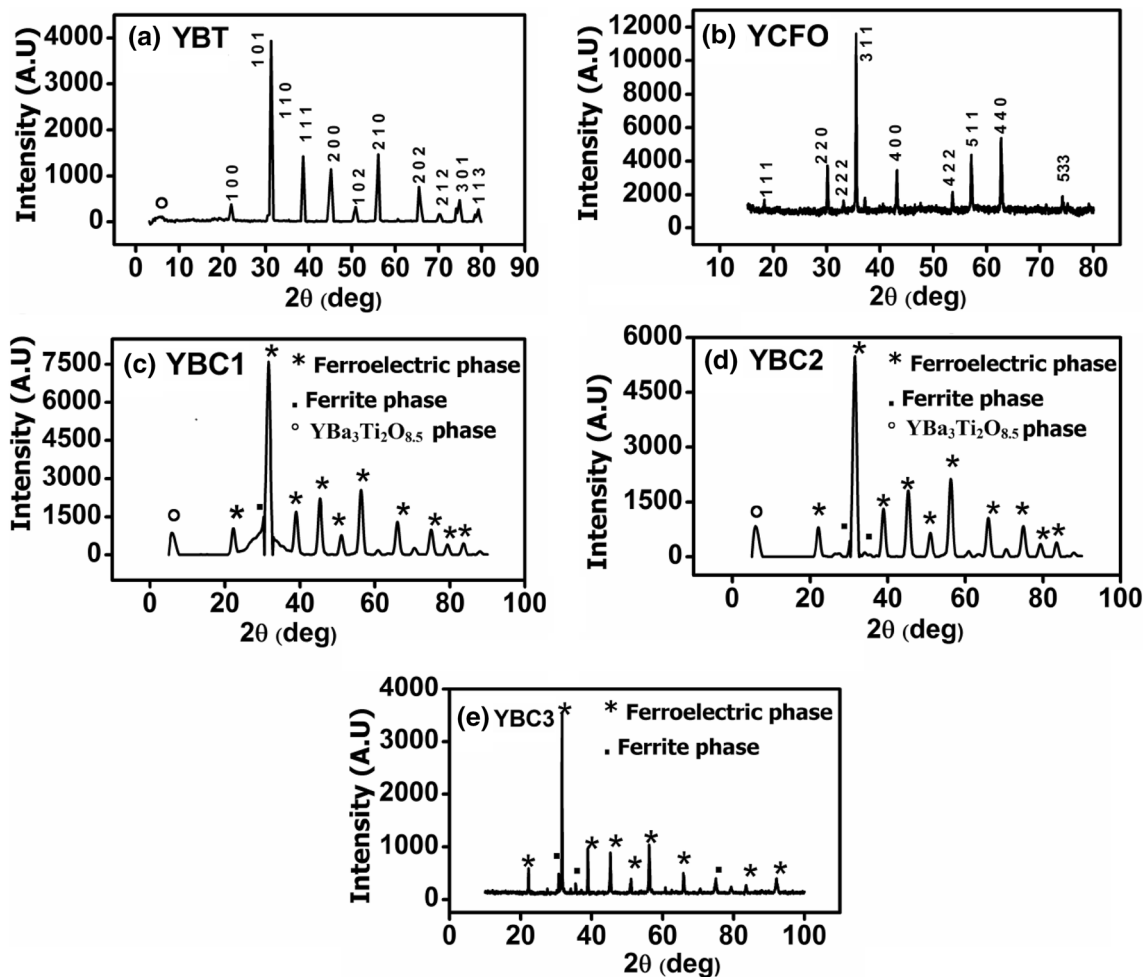


Fig. 1 X-ray diffraction patterns (a) YBT (b) YCFO (c) YBC1 (d) YBC2 and (e) YBC3

multiferroic composite, tabulated in Table 1, were calculated by using the following equations:

$$\text{Phase percentage of YCFO} = \frac{I_{\text{YCFO}}}{I_{\text{YCFO}} + I_{\text{YBT}}} \times 100 \quad (1)$$

$$\text{Phase percentage of YBT} = \frac{I_{\text{YBT}}}{I_{\text{YBT}} + I_{\text{YCFO}}} \times 100 \quad (2)$$

where  $I_{\text{YBT}}$  and  $I_{\text{YCFO}}$  are high intense peaks of YBT and YCFO phases respectively. The obtained values of phase fractions (%) of individual ferroic phases are consistent with the weight fraction of YBT and YCFO taken during synthesis. Although the XRD patterns of composites resemble with each other, however, the relative intensity of all peaks corresponding to YBT phase decreases with the increase in ferrite content. This confirms that two phases coexist in composites.

## 4.2 Microstructure, elemental composition and evaluation of densities

The SEM micrographs of YBT phase and that of composites (YBC1, YBC2 and YBC3) are shown in Fig. 2(a–d). A uniform grain growth is seen for YBT phase and an increase in density ( $4.8 \text{ g/cm}^3$ ) is observed as compared to pure barium titanate [24]. A homogeneous microstructure is observed in all the composites. By increasing the YCFO ferrite phase in composites, the microstructure is found to become denser, supported by the decrease in grain size as tabulated in Table 1. The average grain size was calculated by using IMAGE-J software. EDS analysis was also carried out for YBC1, YBC2 and YBC3 composites to ascertain the presence of doped rare earth ion ( $\text{Y}^{3+}$ ) and other various elements. From Fig. 3, it is clear that all the elements are present in all composites taken during synthesis.

The porosity (P), bulk ( $\rho_{\text{B}}$ ) and X-ray densities ( $\rho_{\text{X}}$ ) were evaluated from the procedure discussed in our earlier work [24]. From these calculations, it was revealed that the density increases with the increase in YCFO phase in the

**Table 1** Density, porosity, lattice parameters and phase fraction of YBT, YCFO, YBC1, YBC2 and YBC3

Sample	$\rho_{\text{B}}$ ( $\text{g/cm}^3$ )	$\rho_{\text{X}}$ ( $\text{g/cm}^3$ )	P (%)	Grain size ( $\mu\text{m}$ )	Lattice parameters		% Phase	
					A	C	YCFO	YBT
YBT	4.8	5.89	18.5	5.0838	3.996	4.032	–	–
YCFO	4.79	5.23	8.41	0.1629	8.3785	–	–	–
YBC1	4.93	5.26	6.27	3.7141	–	–	4.74	95.26
YBC2	4.97	5.29	6.04	2.4398	–	–	10.77	89.23
YBC3	5.31	5.58	4.84	2.0546	–	–	13.46	86.54

**Fig. 2** SEM micrographs (a) YBT, (b) YBC1, (c) YBC2 and (d) YBC3

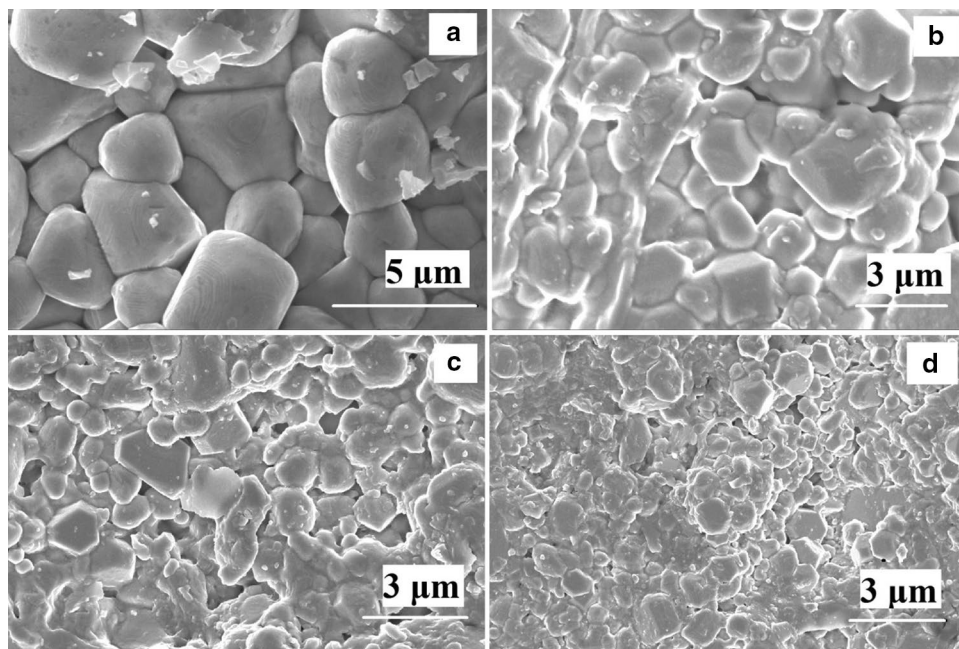
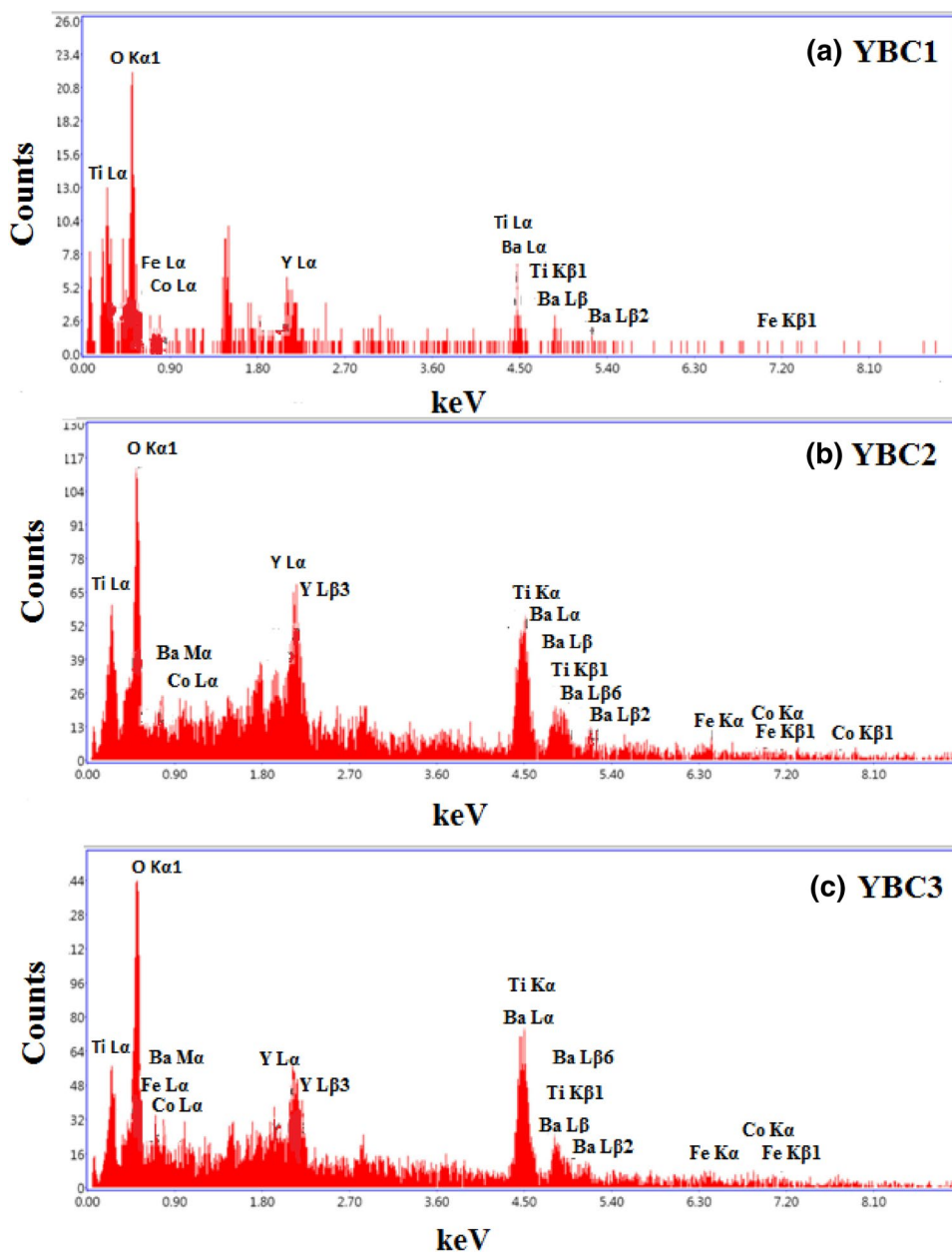


**Fig. 3** EDAX spectrograms (a) YBC1, (b) YBC2, and (c) YBC3



YBT-YCFO composite as depicted in Table 1, consistent with the SEM studies.

### 4.3 Dielectric studies

#### 4.3.1 Variation of dielectric properties with frequency

The variation of dielectric constant ( $\epsilon'$ ) as a function of frequency (2–3 MHz) at room temperature for YBC1, YBC2 and YBC3 is depicted in Fig. 4. It may be noted that the value of  $\epsilon'$  decreases in all composites as compared to that of pure YBT phase. A favourable decrease in the value of  $\epsilon'$  in all composites is attributed to incorporation of YCFO

ferrite phase in the ferroelectric YBT matrix, consistent with earlier studies [20, 25].

At lower frequency (20 Hz), the values of  $\epsilon'$  for all composites is high, depicted in Table 2, and this decreases with increase in frequency up to 6 kHz. Above this frequency range, the value of  $\epsilon'$  shows weak dependence on the frequency of the applied field. In composites, the high value of  $\epsilon'$  at lower frequencies is explained by Maxwell–Wagner-type interfacial polarization [26, 27] in agreement with Koop's phenomenological theory [28]. The uncompensated charges (space charges) at the interface of two ferroic phases are generated due to the difference in their conductivities. At low frequencies, the interfacial polarization developed due to these space charges leads to a high

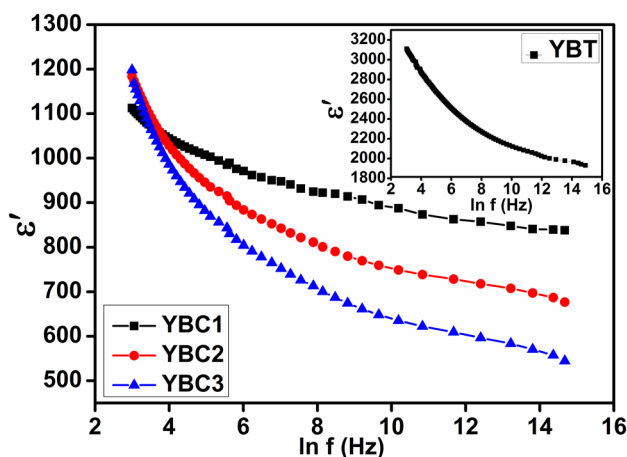


**Fig. 4** Frequency dependence of dielectric constant ( $\epsilon'$ ) for YBC1, YBC2 and YBC3. The inset shows the variation of  $\epsilon'$  with frequency for YBT phase

value of dielectric constant. Further, with increase in ferrite content, an increase in the value of  $\epsilon'$  is found at lower frequencies for YBC3 as compared to YBC1. This increase is explained on the basis of polarization mechanism in ferrites [29], as the  $\text{Fe}^{2+}$  and  $\text{Fe}^{3+}$  ions make the YCFO ferrite phase dipolar. The orientation polarization is developed due to the rotational displacement of  $\text{Fe}^{3+} \leftrightarrow \text{Fe}^{2+}$  dipoles; where electron exchange takes place between  $\text{Fe}^{2+}$  and  $\text{Fe}^{3+}$  ions. These dipoles align themselves with the alternating applied field and hence enhance the dielectric constant. However, at higher frequencies, the exchanging electrons are not able to follow the frequency of the applied field; hence it becomes difficult for them to stay at the grain boundaries, resulting in lower values of dielectric constant.

The variation of dielectric loss ( $\tan \delta$ ) with frequency shows similar behaviour as that of  $\epsilon'$  depicted in Fig. 5. The high value of  $\tan \delta$  at lower frequencies is attributed to space charge polarization [30]. However, at higher frequencies, the process of accumulation of charges at the interfaces is negligible, so  $\tan \delta$  is small. Further, the  $\tan \delta$  increases with the increase in YCFO phase due to conducting nature of YCFO ferroic phase. A loss peak is observed for YCFO phase at a frequency of  $10^9$  Hz as depicted in inset of Fig. 5. The occurrence of loss peak is attributed to the fact that the

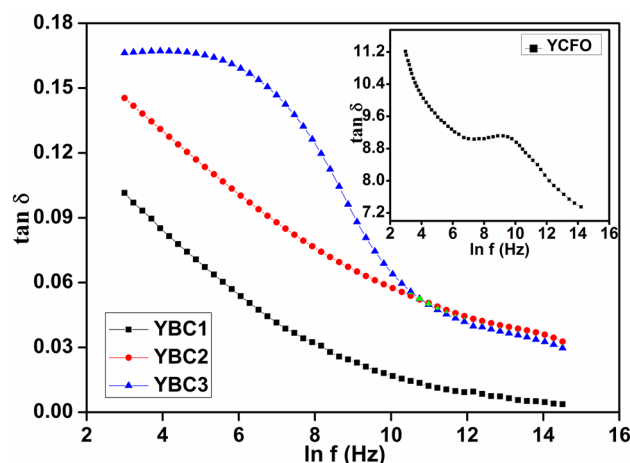


**Fig. 5** Frequency dependence of  $\tan \delta$  for YBC1, YBC2 and YBC3. The inset shows the variation of  $\tan \delta$  with frequency for YBT phase

frequency of the applied field has the same period of relaxation for a particular polarization process.

### 4.3.2 Variation of dielectric properties with temperature

Figure 6(a–d) shows the variation of  $\epsilon'$  as a function of temperature for YBT phase, YBC1, YBC2 and YBC3 composites. A structural phase transition at a temperature ( $T_{C1}=355\text{K}$ ) was observed for YBT suggesting the normal behavior of ferroelectrics. The drop in Curie temperature is observed from 393 to 355K by incorporating yttrium ( $x=0.05\%$ ) in the barium titanate lattice. This is attributed to the fact that for higher dopant concentration,  $\text{Y}^{3+}$  ions tend to occupy B sites rather than A-sites. Since the ionic radius of  $\text{Y}^{3+}$  ( $1.04 \text{ \AA}$ ) is large as compared to  $\text{Ti}^{4+}$  ( $0.74 \text{ \AA}$ ), so the replacement of  $\text{Y}^{3+}$  for  $\text{Ti}^{4+}$  in B-sites may suppress the oriented displacement of B-site ions in the oxygen octahedrons, which are responsible for the spontaneous polarization. Further, the interactions between B-site ions and  $\text{O}^{2-}$  become weaker and this suppression effect results in the drop of  $T_c$ . This drop in  $T_c$  agrees well with the reported ones [31]. In comparison to YBT, the low temperature dielectric studies of all the composites revealed ferroelectric transitions from cubic to tetragonal and from tetragonal to orthorhombic phase respectively. As reported in the literature [32],

**Table 2** Dielectric constant ( $\epsilon'$ ) and dielectric loss ( $\tan \delta$ ) at different Curie temperatures and frequencies for YBT, YBC1, YBC2 and YBC3

Sample	$\epsilon'$ (20 Hz)	$\epsilon'$ (3M Hz)	$\tan \delta$ (20 Hz)	$\tan \delta$ (3 M Hz)	$\epsilon'$ ( $T_{C2}$ )		$\epsilon'$ ( $T_{C1}$ )		$\tan \delta$ ( $T_{C2}$ )		$\tan \delta$ ( $T_{C1}$ )	
					100 kHz	2 MHz	100 kHz	2 MHz	100 kHz	2 MHz	100 kHz	2 MHz
YBT	3108	1918	–	–	–	–	2036	–	–	–	0.058	–
YBC1	1111	836	0.1004	0.0037	948	824	1152	1042	0.012	0.002	0.035	0.024
YBC2	1187	675	0.1458	0.0323	613	535	798	692	0.025	0.015	0.049	0.038
YBC3	1206	540	0.1666	0.0295	474	398	688	536	0.027	0.013	0.14	0.13

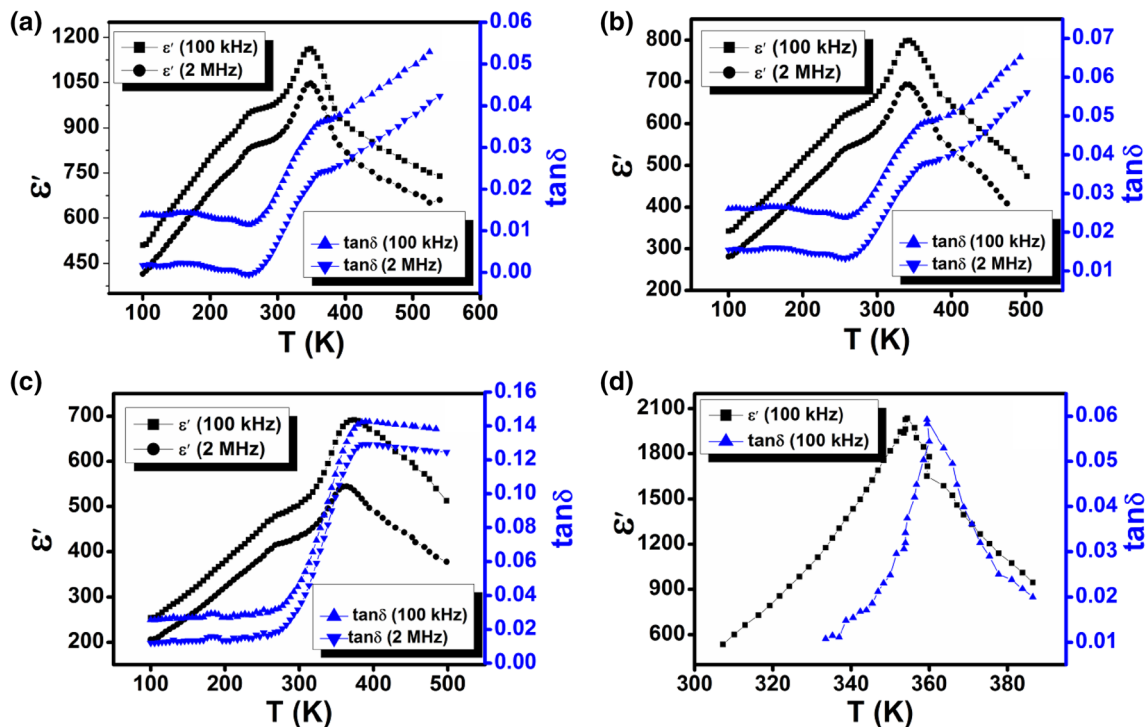


**Fig. 6** Variation of dielectric constant and  $\tan\delta$  with temperature (a) YBC1 (b) YBC2 (c) YBC3 and (d) YBT

in pure barium titanate, the ferroelectric transitions from cubic to tetragonal and tetragonal to orthorhombic occur at ( $T_{C1} = 394$  and  $T_{C2} = 278$  K) respectively. The effect of yttrium doping on the drop of Curie temperature is prominent in all the composites and the values are tabulated in Table 2. Also, the dielectric peak becomes broader and  $T_c$  shifts to higher temperature side with an increase in YCFO phase in composites as compared to pure YBT phase. The higher  $T_c$  for composites is attributed to the lattice deformation of the YBT phase due to diffusion of various ions during the high temperature sintering, consistent with the earlier reports in the literature [33]. The decrease in  $\epsilon'$  was observed with increase in YCFO ferrite phase in the temperature range (100–260 K). This confirms that instead of conducting YCFO phase, the enhanced reversing of polarization contributes to  $\epsilon'$  at low temperatures. This also indicates the existence of ferroelectric nature of all the composites, confirmed by P–E measurements as discussed in Sect. 4.5. In addition, the maximum temperature ( $T_m$ ) is shifted with the increase in frequency in all the composite, confirming relaxor behaviour of all the composites [34].

The variation of  $\tan\delta$  with temperature for YBT shows a similar behaviour as that of  $\epsilon'$ , supporting a ferroelectric phase transition as shown in Fig. 6(d). However, the loss behaviour of composites is quite different than the YBT phase as depicted in Fig. 6(a–c). Although YCFO ferrite phase is conducting, the loss in all the composites is small

over a wide range of temperature (100–550 K), consistent with the earlier reports [35]. At room temperature,  $\tan\delta$  of all composites is small which makes them suitable for device applications. The low loss in composites is attributed to the fact that non-magnetic  $Y^{3+}$  ions, occupying the titanium vacancies, can reduce the number the mobile charge carriers, hence loss is lowered effectively. Above room temperature,  $\tan\delta$  increases rapidly with the increase in temperature. The abrupt rise in  $\tan\delta$  at higher temperatures may be due to the increased hopping rate of electrons between  $Fe^{3+}$  and  $Fe^{2+}$  ions.

#### 4.3.3 Curie–Weiss behaviour

As the peaks around the  $T_{C1}$  are broad, the diffuseness of the phase transitions was determined by modified Curie Weiss law of the form:

$$\frac{1}{\epsilon'} - \frac{1}{\epsilon'_{\max}} = A(T - T_c)^\gamma \quad (3)$$

where  $\gamma$  and  $A$  are assumed to be constants. The parameter  $\gamma$  provides information about the nature of the phase transition. For  $\gamma = 1$ , a normal Curie–Weiss law is obtained suggesting a sharp peak around phase transition and for  $1 < \gamma \leq 2$ , it has a quadratic dependency, which describes a completely diffused phase transition in the paraelectric region. The values of  $\gamma$  are obtained from the slope of  $\ln(1/\epsilon' - 1/\epsilon'_{\max})$

**Fig. 7** Curie Weiss behaviour in paraelectric region (a) YBT (b) YBC1 (c) YBC2 and (d) YBC3

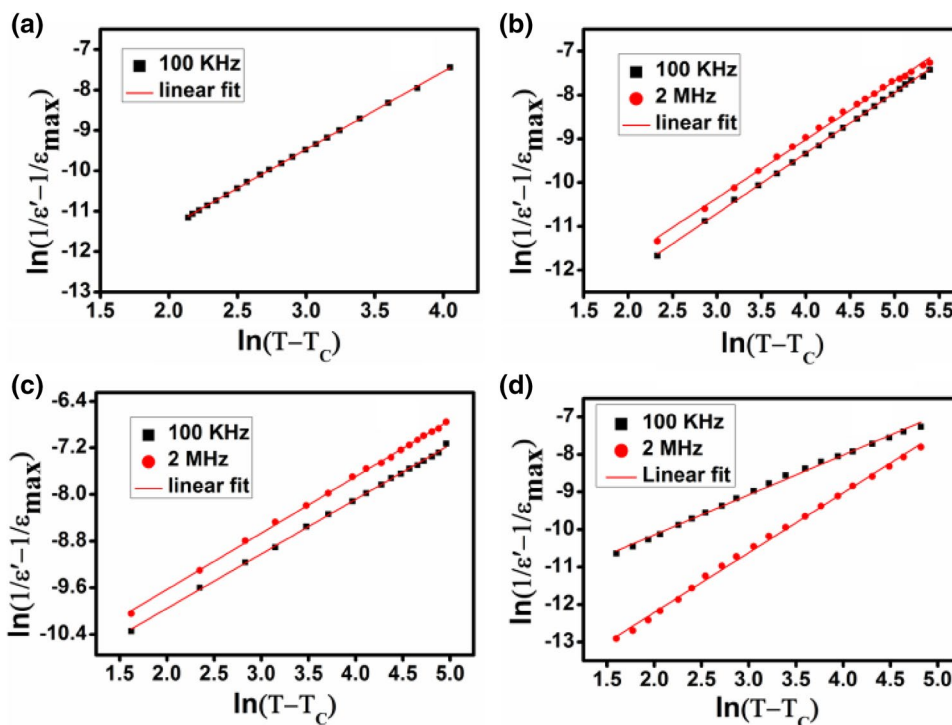


**Table 3** Curie temperatures  $T_{C1}$ ,  $T_{C2}$  and  $\gamma$  for YBT, YBC1, YBC2 and YBC3

Sample	$T_{C1}$ (K)		$T_{C2}$ (K)		$\gamma$	
	100 kHz	2 MHz	100 kHz	2 MHz	100 KHz	2 MHz
YBT	355	–	–	–	1.0643	–
YBC1	342	340	251	251	1.1701	1.1489
YBC2	346	339	255	255	1.3804	1.3389
YBC3	367	360	268	268	1.1721	1.4756

versus  $\ln(T-T_c)$  for YBT phase, YBC1, YBC2 and YBC3 composites as shown in Fig. 7. The obtained values of  $\gamma$  depicted in Table 3, confirmed diffused transition of the composite. The possibility of broadening of the dielectric peak occurs mainly due to the structural disordering and compositional fluctuations in the arrangement of cations in one or more crystallographic sites in the unit cell of the lattice, resulting in microscopic inhomogeneity in the samples with local Curie points [36]. The structural disordering in our case is assumed due to the expansion of the lattice occurring due to replacement of small size  $Ti^{4+}$  ions by large size  $Y^{3+}$  ions [22].

**4.4 Dc conductivity and Motts Law**

In order to check the conducting nature of the composite, the temperature dependent dc conductivity measurements were done. The variation of dc conductivity as a function of temperature is shown in Fig. 8. With increasing temperature, the conductivity is found to increase, indicating semiconducting

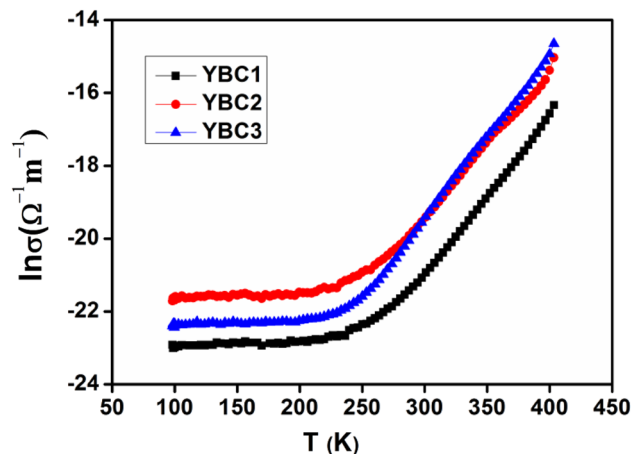


**Fig. 8** Temperature dependence of dc conductivity for YBC1, YBC2 and YBC3



nature. The conductivity of all the composites is due to the ferrite phase, and is explained by the Verwey de Bohr mechanism [37], involving exchange of electrons between the ions of the same type with different valance states. These ions are distributed randomly over equivalent crystallographic lattice sites. In case of spinel ferrites like cobalt ferrite, the  $\text{Fe}^{2+}$  and  $\text{Fe}^{3+}$  ions are distributed over tetrahedral and octahedral sites. The mobile charge carrier is the electron exchanging between  $\text{Fe}^{3+}$  and  $\text{Fe}^{2+}$  ions [38]. The creation of electron exchanging between  $\text{Fe}^{3+}$  and  $\text{Fe}^{2+}$  depends upon the rise in temperature and reduction of  $\text{Fe}^{3+}$  to  $\text{Fe}^{2+}$ , so the conductivity of ferrite is controlled by the  $\text{Fe}^{2+}$  concentration at the octahedral site. In addition, high conductivity was found at higher temperatures for YBC3 in comparison to YBC2 and YBC1 as depicted in Fig. 8. This increase in conductivity with increase in ferrite phase is consistent with the earlier work reported [12, 20, 39].

In YCFO ferroic phase,  $\text{Y}^{3+}$  ions enter the lattice in combination with  $\text{Fe}^{3+}$  ions resulting in a lower concentration of  $\text{Fe}^{2+}$  ions and hence results in decrease in conductivity which is the prime requirement for obtaining a higher ME output. This charge transport via excited states can be expressed as:

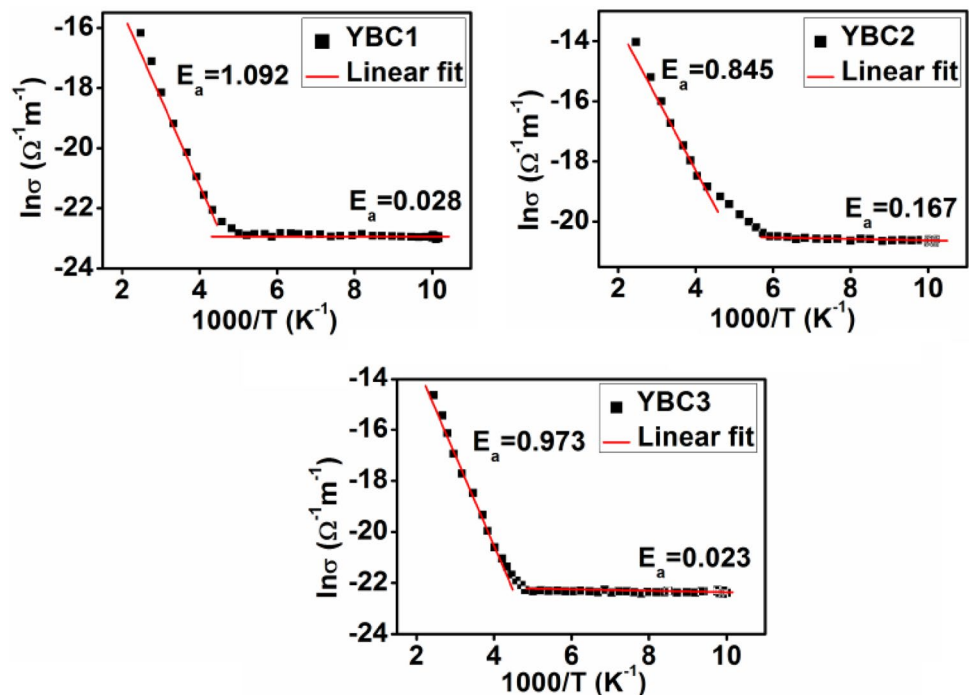
$$\sigma = \sigma_0 \exp^{-E_0/k_B T} + \sigma_1 \exp^{-E_1/k_B T} + \sigma_2 \exp^{-E_2/k_B T} + \dots \quad (4)$$

where  $E_0$  is the activation energy for intrinsic conduction, which arises due to thermal excitation of electrons and  $E_1, E_2, \dots$  are the activation energies needed for hopping conduction.  $\sigma_0, \sigma_1$  and  $\sigma_2$  are constants and  $k_B$  is Boltzmann's constant

[40, 41]. Figure 9 shows the  $\log(\sigma_{dc})$  versus  $1000/T$  plots for all the composites. The activation energy ( $E_a$ ) values in different temperature ranges 400–225 and 225–100 K were calculated. The values of  $E_a$  are higher above the temperature of 225 K and lower below the temperature of 225 K. The higher values of  $E_a$  and increase in conductivity in the temperature range of 225–400 K indicate the semiconducting behaviour for all the composites. However, at low temperatures (225–100 K), the conductivity, as well as  $E_a$  values are small, confirming the metallic nature [42]. The decrease in activation energy at low temperatures in ferrites and perovskites has been explained by small-polaron theory [41, 43]. The small values of  $E_a$  in the lower temperature range (225–100K), suggest that the electronic process that is dominant for the process of conduction, occur in a narrow energy band. Since, the electronic states at lower temperatures are localized, so the transport of charge requires a conduction mechanism through localized states i.e. hopping conduction mechanism. The hopping conduction itself can occur by nearest neighbour hopping or by variable range hopping. The confirmation of hopping conduction mechanism in all the composites was supported by the variable range hopping theory of Mott [44]. As per Mott's theory, if the conduction between localized states near the Fermi level is by hopping, then conductivity has a temperature dependence of the form given by the relation:

$$\sigma = \sigma_0 \exp\left(-\frac{T_0}{T}\right)^{1/4} \quad (5)$$

**Fig. 9** Plot of  $\log \sigma$  versus  $1000/T$  for YBC1, YBC2 and YBC3



From the plots of  $\ln(\sigma)$  vs  $(1/T)^{1/4}$  as depicted in Fig. 10, it is clear that YBC1, YBC2 and YBC3 obeys Mott's law, confirming variable range hopping.

### 4.5 Ferroelectric properties

The polarization–electric field (P–E) hysteresis loops were traced in order to ascertain the ferroelectric behaviour of the YBT phase and composites as depicted in Fig. 11(a). A typical hysteresis loop is observed for YBT ferroic phase with a saturation polarization  $9.25 \mu\text{C}/\text{cm}^2$ . The unsaturated loops were traced for the YBC1, YBC2 and YBC3 composite, withstanding low field due to conducting nature of YCFO phase as compared to YBT phase. The symmetry of loops in YBT phase as well of composites

is attributed to the fact that the internal field developed by bound electrons is negligible as compared to external applied field. Both the saturation polarization ( $P_s$ ), remnant polarization ( $P_r$ ) decreases with an increase of YCFO ferrite content. This decrease in various electric parameters in the composites is due to dilution of ferroelectric properties by the addition of the magnetic YCFO phase. The value of coercivity ( $E_c$ ) in composites is less as compared to YBT phase as depicted Fig. 11(b). This decrease may be due to the symmetrical distribution of YCFO phase in the YBT matrix [45]. However, with the increase of ferrite content, a decrease in the values of coercivity is observed in the composites and agrees well with the literature [46]. Since the ferrites are conductive and could not withstand high voltages, no P–E loop was observed for YCFO phase.

Fig. 10 Plot of  $\log\sigma$  versus  $T^{-1/4}$  for YBC1, YBC2 and YBC3

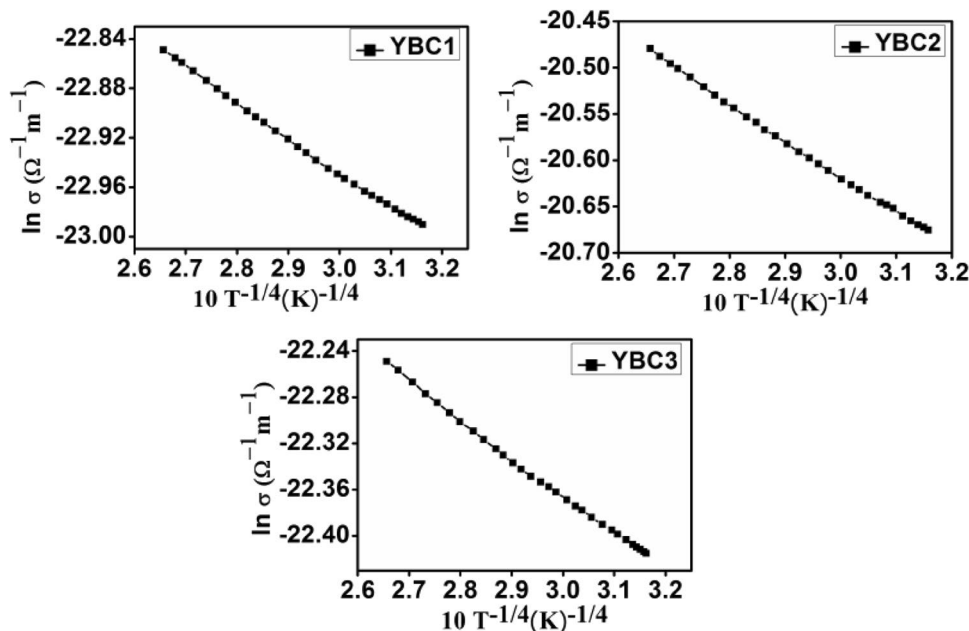
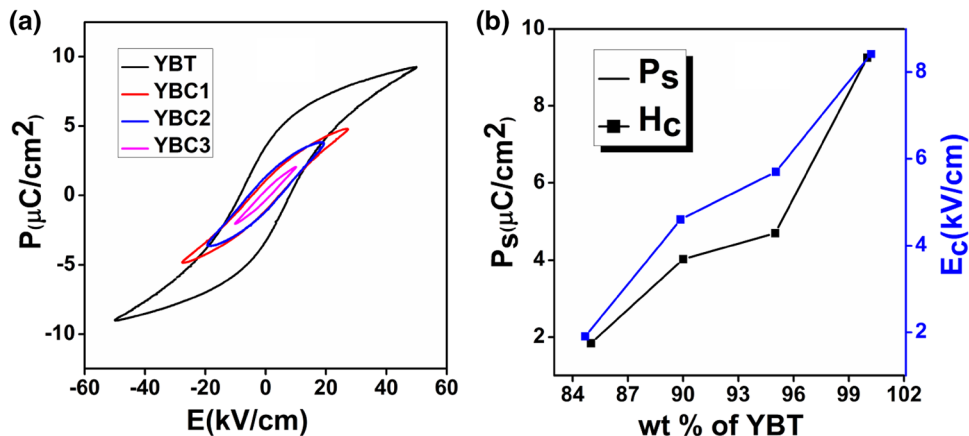


Fig. 11 (a) Room temperature P–E hysteresis loops for YBC1, YBC2 and YBC3. (b) Variation of  $P_s$  and  $H_c$  with the weight content of YBT phase



## 4.6 Magnetic properties

The various magnetic parameters such as coercivity ( $H_c$ ), remanence ( $M_r$ ) and saturation magnetization ( $M_s$ ) of YBC1, YBC2 and YBC3 composites were determined from room temperature magnetic hysteresis by using a VSM with an applied field having range  $-20 \text{ kOe} \leq H \leq 20 \text{ kOe}$  as depicted in Fig. 12(a). For YCFO ferroic phase, a typical hysteresis loop was obtained as depicted in the inset of Fig. 12(a); however in composites unsaturated loops were observed. Although the two ferroic phases act independently in the multiferroic composites due to spinodal decomposition; however, the decrease in magnetic parameters with the increase of ferroelectric phase is due to domain pinning. This domain pinning puts constraint on domain wall motion of the magnetic YCFO phase in composites, and results in unsaturated hysteresis loops with reduced magnetic parameters. Such type of unsaturated loops has been reported in the literature for higher concentrations of ferroelectric phase [47, 48]. Although in composites, the decrease of magnetic parameters as compared to YCFO ferroic phase originates from the migration of  $\text{Fe}^{3+}$  into the B-site, as nonmagnetic  $\text{Y}^{3+}$  prefers to go to the A-site, which leads to superficial spin canting, spin pinning, or broken exchange bonds [49, 50]. In addition to  $\text{Y}^{3+}$  ions, the area of YCFO nano-grains are percolated by a large number of small YBT micro grains, causing an increase in number of voids at the interface, and hence the magnetic properties of YBT-YCFO composite are not only dependent on percentage of YCFO phase but also on area of contact between the grains of two ferroic phases [51]. The maximum coercivity of YCFO phase occurs within its single domain range, with squareness ratio ( $M_r/M_s = 0.52$ ). However, coercivity decreases with increase in YBT ferroelectric phase in composites as depicted in Fig. 12(b). This decrease in coercivity is attributed to the fact that the grains subdivide into multi-domains [52], supported by squareness ratios, shown in Table 4.

From room temperature studies, it is clear that the various magnetic parameters like  $H_c$  and  $M_s$  for all composites have been diluted by the ferroelectric YBT phase. As

**Table 4** Calculated values of magnetic parameters ( $M_r$ ,  $M_s$ ,  $H_c$ ) at room temperature

Sample	$M_r$ (emu/g)	$M_s$ (emu/g)	$H_c$ (Oe)	$M_r/M_s$
YCFO	41.70	79.05	1074.5	0.52
YBC1	0.0024	0.08	159.79	0.03
YBC2	0.0048	0.24	177.11	0.02
YBC3	0.2695	2.45	387.54	0.11

the cobalt ferrite shows an anomalous behaviour below 150 K [53–55], the low-temperature study of YBC3 was done to check the variation of  $H_c$  and  $M_s$  with temperature. Figure 13(a) shows the  $M$ – $H$  loops of YBC3 over a wide temperature range (293–123 K). It is clear that as the temperature is increased, the area of hysteresis loop decreases, causing a drop in  $M_s$  values. The minimum value of  $M_s$  is observed at 300 K, which is attributed to the fact that at room temperature, thermal fluctuation may decrease super-exchange interaction between cations which results in drop of the saturation magnetization [56]. In addition, coercivity was found to increase with a decrease in temperature as shown in Fig. 13(b), which is attributed to increasing of anisotropy field [57]. At low temperatures, thermal energy is not enough to overcome the magnetic energy, resulting in frozen spins and hence enhances coercivity.

## 4.7 Magneto-electric coupling

The magnetodielectric phenomenon is an indirect way to investigate the magneto-electric coupling in the composites. The magnetodielectric (MD) effects in composite materials may be due to several reasons which include magnetostriction effect, magnetoresistance or magneto-electric coupling. The magnetostriction is due to change in lattice parameters by the application of an applied magnetic field. In presence of magnetic field, the system gets strained, which propagates and induces stress. As there is coupling between the ferroelectric and ferrite domains, this induced stress generates an electric field on the ferroelectric domain via the ME effect

**Fig. 12** (a) Room temperature  $M$ – $H$  hysteresis loops for YBC1, YBC2 and YBC3, with inset showing  $M$ – $H$  loop of YCFO phase (b) Variation of  $M_s$  and  $H_c$  with the weight percentage of YBT phase, with inset showing a variation of squareness ratio (SR) with the weight percentage of YCFO phase

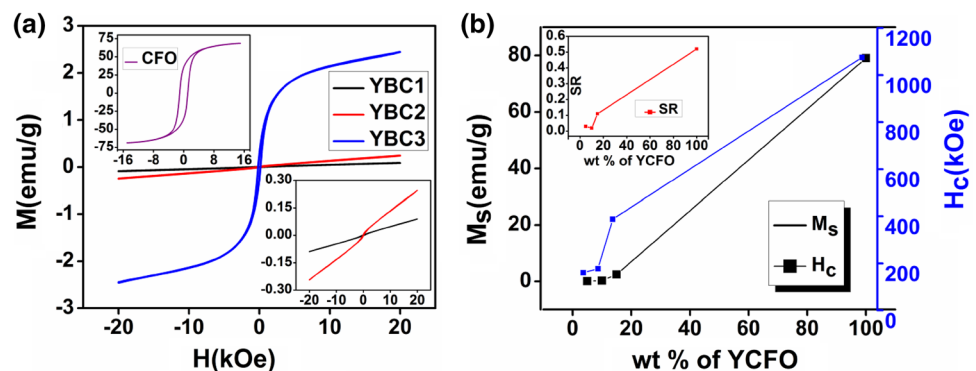


**Fig. 13** (a) Low-temperature M–H loops for YBC3 phase. (b) Variation of  $M_S$  and  $H_C$  with temperature

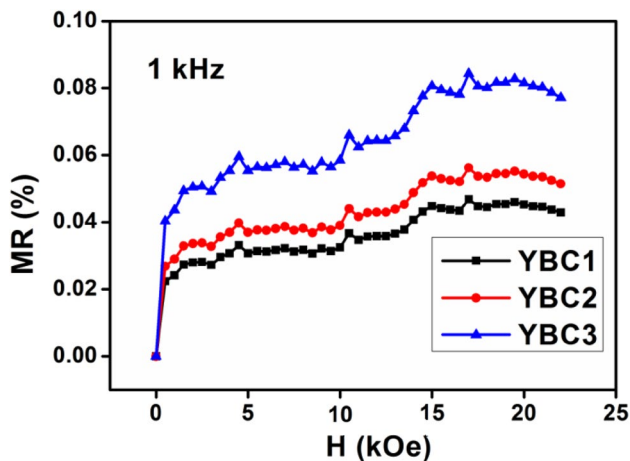
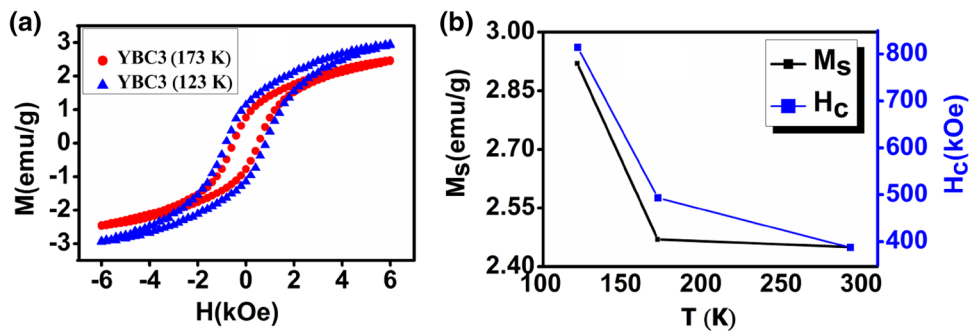


**Fig. 14** Variation of MR (%) with the applied magnetic field for YBC1, YBC2 and YBC3

[58], hence modifying the dielectric behavior. Since the MD effect may be due to magnetoresistance of the composite, so firstly we calculated the fractional change in resistivity by the application of applied magnetic field as shown in Fig. 14, at a frequency of 1 kHz by using relation:

$$MR = \frac{\rho(H) - \rho(H = 0)}{\rho(H = 0)} \times 100 \tag{7}$$

where  $\rho(H)$  and  $\rho(0)$  represent the value of the dielectric constant in the presence and absence of magnetic field (H)

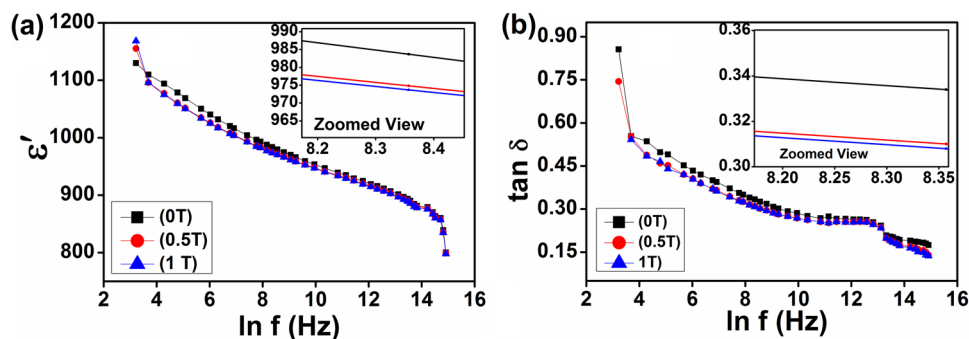
respectively. The value of magnetoresistance for YBC1, YBC2 and YBC3 were calculated, and was found to be 0.043%, 0.051% and 0.077% respectively. This confirms that the magnetoresistance contributes to the MD effect in the composites.

Since the magnetoresistance is small, so this may not be the only reason for magnetodielectric phenomenon. In multiferroic materials, an applied magnetic field not only disturbs the magnetic order, but also changes the dielectric constant [59]. This change is brought about by magnetostriction effect which is another reason for the magnetodielectric phenomenon. Thus in order to understand the coupling between the two ferroic phases, we adopted an indirect way of measuring the fractional change in the dielectric constant as a function of the applied magnetic field. Figures 15, 16, 17 shows the variation of  $\epsilon'$  and  $\tan\delta$  of YBC1, YBC2 and YBC3 composites as a function of frequency at different magnetic fields. With an increase in frequency, the  $\epsilon'$  as well as  $\tan\delta$  decreases at a constant magnetic field. However, with the increase in the applied magnetic field,  $\epsilon'$  as well as  $\tan\delta$  were found to decrease for all composites.

As the change is observed in the  $\epsilon'$  with the varying magnetic field, it was thought worthwhile to carry out the magneto-capacitance measurements. The effect of the magnetic field on the dielectric constant i.e. magnetodielectric effect is calculated by using the relation:

$$MC = \frac{\epsilon(H) - \epsilon(H = 0)}{\epsilon(H = 0)} \times 100 \tag{8}$$

**Fig. 15** Variation of (a) dielectric constant ( $\epsilon'$ ) and (b) dielectric loss ( $\tan\delta$ ) as a function of frequency at different magnetic fields for YBC1



where  $\epsilon(H)$  and  $\epsilon(0)$  represent the value of the dielectric constant in the presence and absence of magnetic field (H) respectively.

Figures 18, 19, 20 shows the variation of MC (%) and  $\tan\delta$  of YBC1, YBC2 and YBC3 composites in the applied magnetic field range  $-20\text{kOe} \leq H \leq 20\text{kOe}$ . A small change in MC (%) is observed with increase in the magnetic field

up to a probing frequency of 10 kHz. Above the frequency of 10 kHz, no change was observed in MD response. The MD effect in the low-frequency region ( $f < 10\text{ kHz}$ ) is due to magnetoresistance effect combined with a Maxwell–Wagner effect [59, 60].

The value of the MC(%) of YBC1, YBC2 and YBC3 continuously increase in the negative direction with an

**Fig. 16** Variation of (a) dielectric constant ( $\epsilon'$ ) and (b) dielectric loss ( $\tan\delta$ ) as a function of frequency at different magnetic fields for YBC2

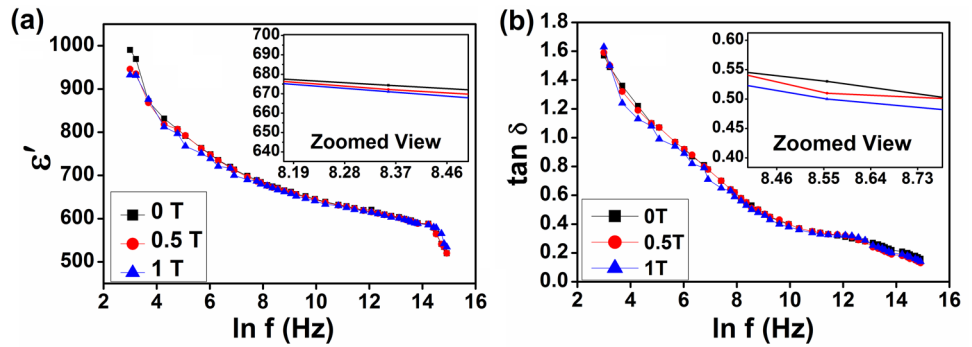


**Fig. 17** Variation of (a) dielectric constant ( $\epsilon'$ ) and (b) dielectric loss ( $\tan\delta$ ) as a function of frequency at different magnetic fields for YBC3

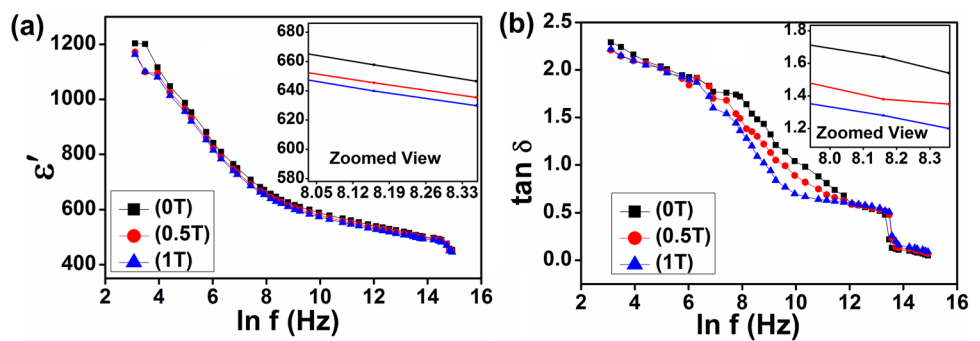


**Fig. 18** Variation of MC(%) as a function of applied magnetic field for YBC1 (a) 500 Hz (b) 1–100 kHz (c) The variation of  $\tan\delta$  as a function of magnetic field for YBC1 at different frequencies

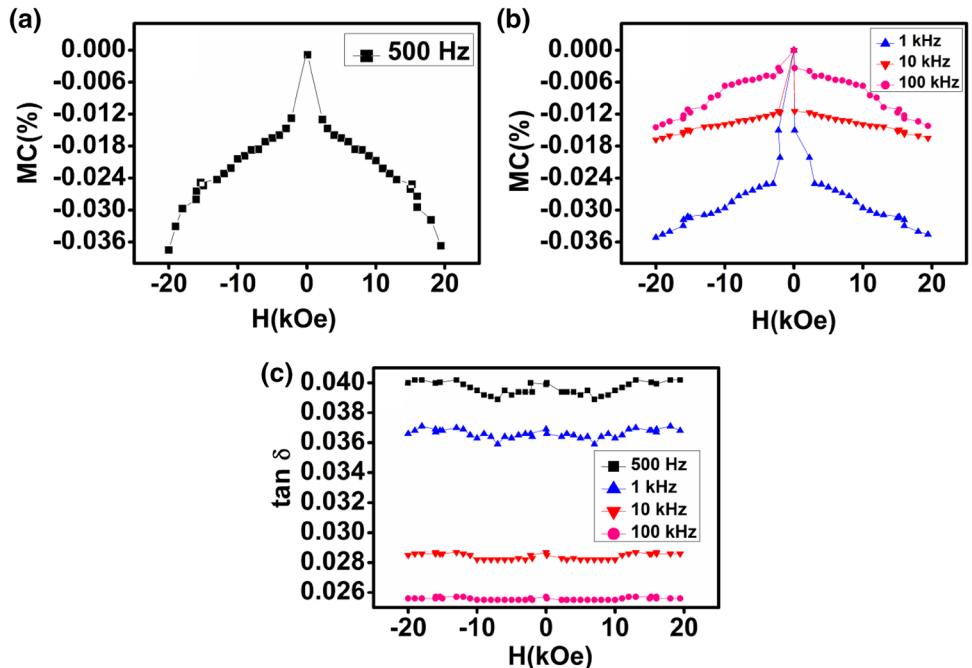


**Fig. 19** Variation of MC(%) as a function of applied magnetic field for YBC2 (a) 500 Hz (b) 1–100 kHz (c) The variation of tanδ as a function of magnetic field for YBC2 at different frequencies

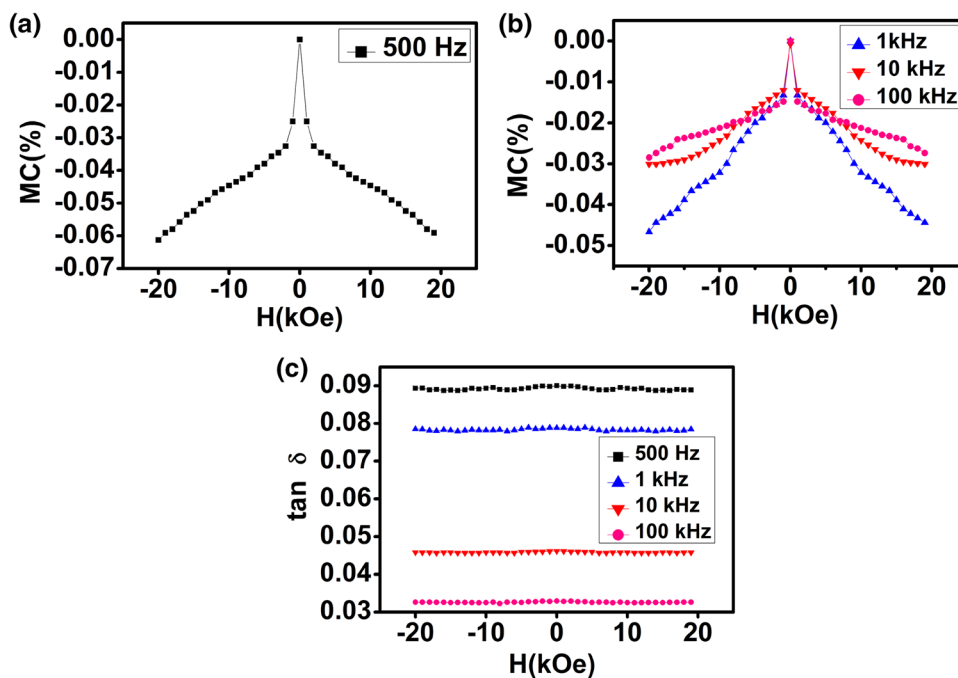
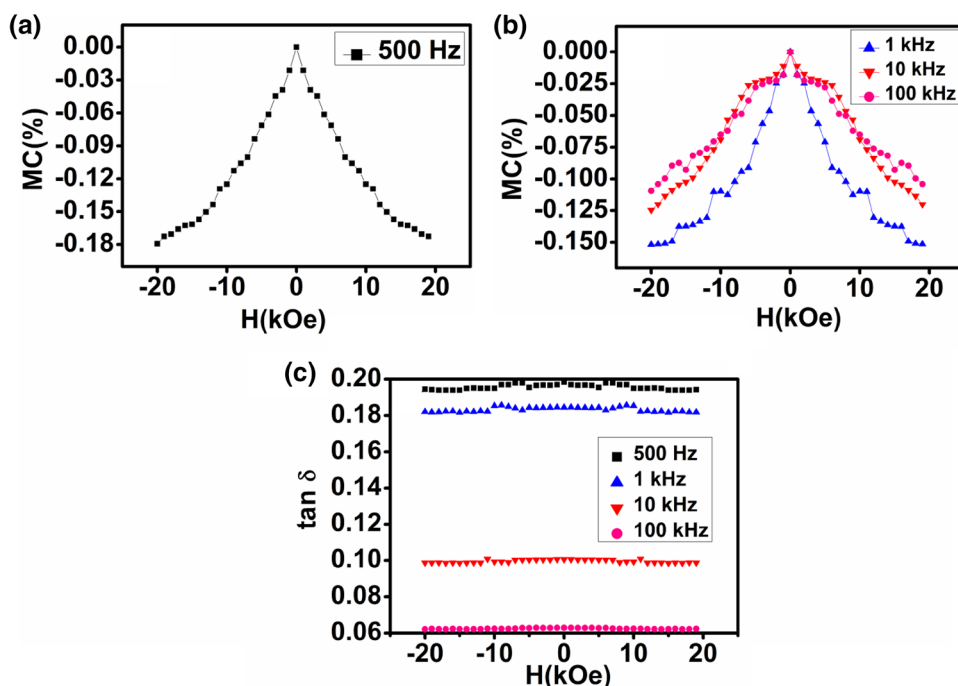


**Fig. 20** Variation of MC(%) as a function of applied magnetic field for YBC3 (a) 500 Hz (b) 1–100 kHz (c) The variation of tanδ as a function of magnetic field for YBC3 at different frequencies



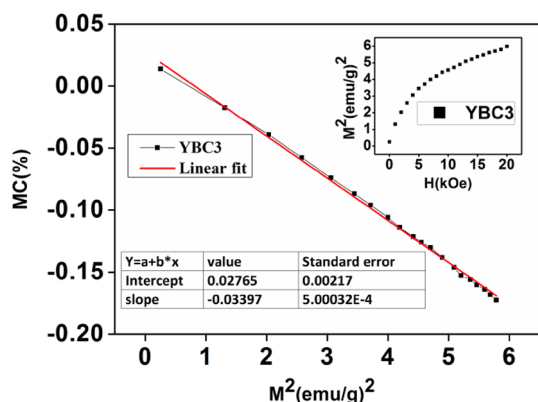
increase in the magnetic field, confirming a negative magnetoelectric coupling. The values of MC(%) for YBC1, YBC2 and YBC3 and dielectric loss at different frequencies are tabulated in Table 5. For all the samples, the average dielectric loss is found to be less than 0.2. A small increase in tanδ was found with the increase of ferrite phase in the composite, attributed to the conducting nature of YCFO phase.

In composites containing both magnetic and ferroelectric phases, the thermodynamic potential  $\varphi$  can be written by the following equation:

$$\varphi = \varphi_o + \alpha P^2 + \frac{\beta}{2} P^4 + \alpha' P^2 - PE - MH + \frac{\beta'}{2} M^4 + \gamma P^2 M^2 \tag{9}$$

**Table 5** Magnetocapacitance, magnetoresistance and  $\tan\delta$  of YBC1, YBC2 and YBC3 at different frequencies

	YBC1				YBC2				YBC3			
	500 Hz	1 kHz	10 kHz	100 kHz	500 Hz	1 kHz	10 kHz	100 kHz	500 Hz	1 kHz	10 kHz	100 kHz
Frequency	500 Hz	1 kHz	10 kHz	100 kHz	500 Hz	1 kHz	10 kHz	100 kHz	500 Hz	1 kHz	10 kHz	100 kHz
MC (%)	0.0318	0.0358	0.0145	0.0168	0.0616	0.0468	0.0288	0.0288	0.1806	0.1532	0.1093	0.1223
MR (%)	–	0.043	–	–	–	0.051	–	–	–	0.071	–	–
$\tan\delta_{av}$	0.0402	0.0371	0.0287	0.0257	0.09	0.0788	0.0461	0.0366	0.1988	0.1855	0.1006	0.0629

**Fig. 21** variation of MC (%) with  $M^2$  and inset shows the variation of  $M^2$  with H for YBC3

where  $M$  and  $P$  are the order parameters for the magnetization and the polarization respectively. The constants  $\alpha$ ,  $\beta$ ,  $\alpha'$ ,  $\beta'$  and  $\gamma$  are coupling coefficients. The last term ( $P^2M^2$ ) represents the interaction between magnetic and ferroelectric phases of the multiferroic composite. In order to calculate coupling coefficients, Kimura et al [61] used the free energy expression, wherein, the effect of magnetic ordering on the change in dielectric constant is proportional to the square of magnetization i.e.  $\Delta\epsilon' \sim \gamma M^2$ . Depending upon the sign of magnetodielectric interaction ( $\gamma$ ), the value of  $\Delta\epsilon'$  can be either positive or negative. Instead of dielectric constant, we are here interested in magnetocapacitance, so the variation of MC (%) as a function of the square of magnetization ( $M^2$ ) is depicted in Fig. 21 for YBC3 composite and the corresponding variation of  $M^2$  with the applied magnetic field (H) are shown in the inset of Fig. 21. It is clear from the plot that the MC(%) varies linearly with  $M^2$  and can be expressed as  $MC(\%) \sim \gamma M^2$ . The magnetoelectric coupling coefficient for YBC3 was calculated by a linear fit to this formula and the obtained value is  $3.397 \times 10^{-2} (\text{emu/g})^{-2}$ .

## 5 Conclusion

In this report, a systematic studies was done on structural, dielectric, ferroelectric, magnetic and magnetodielectric properties of  $x\text{CoY}_{0.1}\text{Fe}_{1.9}\text{O}_4-(1-x)\text{Ba}_{0.95}\text{Y}_{0.05}\text{TiO}_3$

( $x=0.05, 0.1$  and  $0.15$ ) multiferroic composites. The XRD studies revealed that the individual phases retain their crystal structure in all the composites. The SEM images show a uniform distribution of individual phases in the composite and decrease in grain size was observed with increase in ferrite content. The dielectric studies revealed a diffused phase transition for both YBT and composites. The room temperature ferroelectric studies revealed saturated P–E loops for YBT phase and composites, however reduction in ferroelectric parameters was observed in composites due to the incorporation of YCFO phase. The dilution of various magnetic parameters was observed in composites due to domain pinning by non-magnetic YBT phase. Low-temperature magnetic studies showed enhanced coercivity for  $x=0.15$ , as the spins get frozen. From magnetodielectric studies, a favourable increase in percentage magnetocapacitance was observed at lower frequencies for all composites. The magnetoelectric coupling coefficient was calculated for  $x=0.15$  and found to be  $3.397 \times 10^{-2} (\text{emu/g})^{-2}$ .

**Acknowledgements** The authors are thankful to Ms. Rosy Rahman, Ph.D Research Scholar, IIT Kharagpur for providing XRD and FESEM facility. The authors also thank authorities of the University of Kashmir for providing facility of the vibrating sample magnetometer facility (Micro Sense EZ9 VSM) for magnetic measurements.

## References

1. C. Schmitz-Antoniak, D. Schmitz, P. Borisov, F.M. De Groot, S. Stienen, A. Warland, B. Krumme, R. Feyerherm, E. Dudzik, W. Kleemann, H. Wende, Nat. Commun. **4**, 2051 (2013)
2. B. Li, C. Wang, G. Dou, Cryst. Eng. Comm. **15**(11), 2147–2156 (2013)
3. K.C. Verma, R.K. Kotnala, N.S. Negi, Appl. Phys. Lett. **92**(15), 152902 (2008)
4. D. Khomskii, Physics **2**, 20 (2009)
5. G. Catalan, J.F. Scott, Adv. Mater. **21**(24), 2463–2485 (2009)
6. C.W. Nan, M.I. Bichurin, S. Dong, D. Viehland, G. Srinivasan, J. Appl. Phys. **103**(1), 031101 (2008)
7. M.U.D. Rather, R. Samad, B. Want, J. Electron. Mater. **47**(3), 2143–2154 (2018)
8. K. Kageyama, J. Takahashi, J. Am. Ceram. Soc. **87**(8), 1602–1605 (2004)
9. K.D. Schomann, Appl. Phys. **6**(1), 89–92 (1975)
10. Y.H. Tang, X.M. Chen, Y.J. Li, X.H. Zheng, Mater. Sci. Eng. B **116**(2), 150–155 (2005)
11. Y. Shen, J. Sun, L. Li, Y. Yao, C. Zhou, R. Sua, Y. Yang, J. Mater. Chem. C **2**(14), 2545–2551 (2014)

12. R. Sharma, P. Pahuja, R.P. Tandon, *Ceram. Int.* **40**(7), 9027–9036 (2014)
13. M. Etier, V.V. Shvartsman, Y. Gao, J. Landers, H. Wende, D.C. Lupascu, *Ferroelectrics* **448**(1), 77–85 (2013)
14. M.T. Buscaglia, M. Viviani, V. Buscaglia, C. Bottino, P. Nanni, *J. Am. Ceram. Soc.* **85**(8), 1569–1575 (2002)
15. P. Yongping, Y. Wenhui, C. Shoutian, *J. Rare Earths* **25**, 154–157 (2007)
16. A. Franco Jr., H.V.S. Pessoni, T.E.P. Alves, *Mater. Lett.* **208**, 115–117 (2017)
17. B. Sarkar, B. Dalal, V. Dev Ashok, K. Chakrabarti, A. Mitra, S.K. De, *J. Appl. Phys.* **115**(12), 123908 (2014)
18. N. Pulphol, R. Muanghlua, S. Niemcharoen, N. Vittayakorn, W. Vittayakorn, *Ferroelectrics* **488**(1), 170–180 (2015)
19. K.C. Verma, S. Singh, S.K. Tripathi, R.K. Kotnala, *J. Appl. Phys.* **116**(12), 124103 (2014)
20. R. Samad, M.U.D. Rather, B. Want, *J. Alloys Compd.* **715**, 43–52 (2017)
21. M. Fechner, S. Ostanin, I. Mertig, *Phys. Rev. B* **77**(9), 094112 (2008)
22. P. Ren, Q. Wang, X. Wang, L. Wang, J. Wang, H. Fan, G. Zhao, *Mater. Lett.* **174**, 197–200 (2016)
23. A. Chena, Z. Yu, V.M. Ferreira, P.M. Vilarinho, J.L. Baptista, *J. Eur. Ceram. Soc.* **16**(10), 1051–1056 (1996)
24. B. Want, M.U.D. Rather, R. Samad, *J. Mater. Sci.* **27**(6), 5860–5866 (2016)
25. X. Qi, J. Zhou, Z. Yue, Z. Gui, L. Li, S. Buddhudu, *Adv. Funct. Mater.* **14**(9), 920–926 (2004)
26. J.C. Maxwell, *Electricity and Magnetism* (Oxford University Press), Oxford, 1973)
27. K.W. Wagner, *Ann. Phys.* **40**, 818 (1993)
28. C.G. Koops, *Phys. Rev. B* **83**(1), 121 (1951)
29. T.G. Lupeiko, I.B. Lopatina, I.V. Kozyrev, L.A. Derbaremdiker, *Inorg. Mater.* **28**(3), 481–485 (1992)
30. V. Senthil, T. Badapanda, S.N. Kumar, P. Kumar, S. Panigrahi, *J. Polym. Res.* **19**(3), 9838 (2012)
31. D. Shana, Y.F. Qua, J.J. Song, *Solid State Commun.* **141**(2), 65–68 (2007)
32. K.K. Chi, *Dielectric phenomena in solids: with emphasis on physical concepts of electronic processes* (2004)
33. R. Maier, J.L. Cohn, J.J. Neumeier, L.A. Bandersky, *Appl. Phys. Lett.* **78**(17), 2536–2538 (2001)
34. S.K. Rout, P.K. Barhai, E. Sinha, *Phase Transit.* **81**(1), 129–137 (2008)
35. Q. Sun, J. Hu, Q. Gu, K. Bian, J. Wang, K. Xiong, K. Zhu, *Mater. Tech.* **31**(14), 854–859 (2016)
36. H.R. Rukmini, R.N.P. Choudary, D.L. Prabhakara, *J. Phys. Chem. Solids* **61**, 1735–1743 (2000)
37. E.J. Verwey, J.H. de Boer, *Rec. Trav. Chim. Pays-Bas.* **55**(6), 531–540 (1936)
38. R.S. Devan, Y.D. Kolekar, B.K. Chougule, *J. Phys.:Condens. Matter* **18**, 9809–9821 (2006)
39. R. Grigalaitis, M.M. Vijatović Petrović, J.D. Bobić, A. Dzunuzovic, R. Sobiestianskas, A. Brilingas, B.D. Stojanović, J. Banys, *Ceram. Int.* **40**(40), 6165–6170 (2014)
40. R.S. Vemuri, K. Kamala Bharathi, S.K. Gullapalli, C.V. Ramana, *ACS Appl. Mater. Interfaces* **2**(9), 2623–2628 (2010)
41. K. Kamala Bharathi, G. Markandeyulu, C.V. Ramana, *J. Electrochem. Soc.* **158**(3), G71–G78 (2011)
42. A. Azam, A. Jawad, A.S. Ahmed, M. Chaman, A.H. Naqvi, *J. Alloys. comp.* **509**(6), 2909–2913 (2011)
43. I.C. Nlebedim, K.W. Dennis, R.W. McCallum, D.C. Jiles, *J. Appl. Phys.* **115**(17), 17A519 (2014)
44. N.F. Mott, *Phil. Mag.* **19**(160), 835–852 (1969)
45. N. Adhlakha, K.L. Yadav, *Smart Mater. Struct.* **2**(11), 115021 (2012)
46. D.K. Pradhan, R.N.P. Chowdhury, T.K. Nath, *Appl. Nanosci.* **2**(3), 261–273 (2012)
47. H. Yang, G. Zhang, Y. Lin, *J. Alloys Compd.* **644**, 390–397 (2015)
48. V.L. Mathe, A.D. Sheikh, G. Srinivasan, *J. Magn. Magn.Mater.* **324**(5), 695–703 (2012)
49. B. Van den, D.R. Terrell, R.A.J. Born, H.F.J. Giller, *J. Mater. Sci.* **9**(10), 1705–1709 (1974)
50. G. Srinivasan, E.T. Rasmussen, R. Hayes, *Phys. Rev. B* **67**(1), 014418 (2003)
51. R.C. Kambalea, P.A. Shaikha, C.H. Bhosalea, K.Y. Rajpurea, Y.D. Kolekarb, *J. Alloys Compd.* **489**(1), 310–315 (2010)
52. N. Preksha, N. Dhruv, S. Solanki, R.B. Kulkarni, Jotania, *AIP Conf. Proc.* **1728**(1), 020074 (2016)
53. Y. Melikhov, J.E. Snyder, D.C. Jiles, A.P. Ring, J.A. Paulsen, C.C.H. Lo, K.W. Dennis, *J. Appl. Phys.* **99**(8), 08R102 (2006)
54. Y. Melikhov, J.E. Snyder, C.C. Lo, P.N. Matlage, S.H. Song, K.W. Dennis, D.C. Jiles, *IEEE Trans. Magn.* **42**(10), 2861–2863 (2006)
55. N. Ranvah, I.C. Nlebedim, Y. Melikhov, J.E. Snyder, P.I. Williams, A.J. Moses, D.C. Jiles, *IEEE Trans. Magn.* **45**(10), 4261–4264 (2009)
56. K. Maaz, M. Usman, S. Karim, A. Mumtaz, S.K. Hasanain, M.F. Bertino, *J. App. Phys.* **105**(11), 113917 (2009)
57. B.D. Cullity, C.D. Graham, *Introduction to Magnetic Materials* (Addison-Wesley, Oxford, 2009)
58. S.N. Babu, J.H. Hsu, Y.S. Chen, J.G. Lin, *J. Appl. Phys.* **109**(7), 07D904 (2011)
59. G. Catalan, *Appl. Phys. Lett.* **88**(10), 102902–102904 (2006)
60. A. Venimadhav, D. Chandrasekar, J. Krishna Murthy, *Appl Nanosci.* **3**(1), 25–28 (2013)
61. T. Kimura, S. Kawamoto, I. Yamada, M. Azuma, M. Takano, Y. Tokura, *Phys. Rev. B* **67**(18), 180401–180404 (2003)